Bringing real-time traceability to high-speed atomic force microscopy

OPEN ACCESS
IOP Publishing
Measurement Science and Technology
Meas. Sci. Technol. **31** (2020) 074005 (11pp)
https://doi.org/10.1088/1361-6501/ab7ca9

Bringing real-time traceability to high-speed atomic force microscopy

Edward Heaps[1], Andrew Yacoot[1], Herve Dongmo[1], Loren Picco[2,3], Oliver D Payton[2], Freddie Russell-Pavier[1,2] and Petr Klapetek[4,5]

[1] National Physical Laboratory, Teddington, Middlesex, TW11 0LW, United Kingdom
[2] University of Bristol, Tyndall Avenue, Bristol, BS8 1TL, United Kingdom
[3] Department of Physics, Virginia Commonwealth University, Richmond, 23284 VA, United States of America
[4] Czech Metrology Institute, Okružní 31, 638 00, Brno, Czech Republic
[5] CEITEC, Brno University of Technology, Purkyňova 123, 612 00 Brno, Czech Republic

E-mail: andrew.yacoot@npl.co.uk

Received 21 January 2020, revised 20 February 2020
Accepted for publication 4 March 2020
Published 27 April 2020

Abstract

In recent years, there has been growth in the development of high-speed AFMs, which offer the possibility of video rate scanning and long-range scanning over several hundred micrometres. However, until recently these instruments have been lacking full traceable metrology. In this paper traceable metrology, using optical interferometry, has been added to an open-loop contact-mode high-speed AFM to provide traceability both for short-range video rate images and large-area scans made using a combination of a high-speed dual-axis scanner and long-range positioning system. Using optical interferometry to determine stages' positions and cantilever displacement enables the direct formation of images, obviating the need for complex post-processing corrections to compensate for lateral stage error. The application of metrology increases the spatial accuracy and linearisation of the high-speed AFM measurements, enabling the generation of very large traceable composite images.

Keywords: metrology, high-speed atomic force microscopy, traceability, nanometrology, nanotechnology

(Some figures may appear in colour only in the online journal)

1. Introduction

The atomic force microscope (AFM) is the workhorse of nanotechnology, with applications in surface imaging, manipulation, materials analysis, lithography and metrology [1]. National metrology institutes (NMIs) have directed considerable effort towards ensuring dimensional measurements made using AFMs can be made traceable to the SI metre via metrological AFMs (MAFMs) [2]. These MAFMs usually use optical interferometry to traceably measure the relative displacement between the AFM tip and sample. They are used primarily for the calibration of transfer artefacts or for investigation of instrumentation and imaging artefacts that affect dimensional measurements using AFMs. These transfer artefacts are used to bring traceability to the AFM community via calibration of commercial AFMs. Although these NMI instruments tend to be slow, in recent years there has been some effort to increase the scan speed of these to 500 μm s^{-1} [3], but they lack the high data density of other forms of high-speed AFM (HS-AFM).

In parallel, outside of NMIs, there has been rapid growth in the use of HS-AFM systems based on a number of different approaches [4–8]. A common feature of many of these systems is a lack of metrology and measurement traceability; instead, the design emphasis has been on obtaining video rate images to observe dynamic processes or gather material

properties from large areas. On the other hand, the diversity of instrument designs, e.g. [7, 9], and general interest in HS-AFM has opened up a new area of AFM technology that is without fully traceable metrology but has a plethora of applications in many areas ranging from healthcare [10] to materials science [4, 11] and life sciences [12].

The aim of this work is to integrate traceable metrology, based on optical interferometry, into the lateral axes of a HS-AFM that can be used both within and outside of an NMI, rather than develop an instrument with top-level NMI performance. The introduction of metrology to a growing field of HS-AFM instrumentation should benefit numerous application areas outside of pure metrology as the dimensional measurements associated with the AFM images will be accurate and have a known uncertainty.

The HS-AFM instrument described in this paper is based on previous designs originating at the University of Bristol (UoB). The operating principles of this configuration of HS-AFM diverge from conventional AFM and some other HS-AFMs by relying on passive mechanical feedback to maintain tip-sample contact as the cantilever moves across the sample at high-speeds [13]. This tip-sample interaction relies on a fluid dynamical lubrication effect that protects both the sample and the resolution achievable using the AFM tip [14] even as the cantilever passes over large features in the absence of a per pixel electromechanical control loop. This effect is only present at high-speed. Thus, this kind of instrument cannot operate in a conventional low-speed mode [13]. Furthermore, it has been shown 15] that with direct measurement of the vertical displacement of the cantilever using an optical vibrometer, in place of the more typical optical beam deflection (OBD), repeatable high-speed metrological imaging is possible.

Previously, the UoB HS-AFM did not use sensors to measure the relative lateral (x–y) movement between the tip and sample during high-speed scans. Instead, it relied on a combination of the driving signals to the high-speed stage, encoders on the coarse positioners and feature recognition. This produced data susceptible to errors caused by hysteresis in the driving piezos, non-ideal motion of the stage itself and stitching errors in post processing.

Initial work between NPL, CMI and UoB [16, 17] showed, that for these AFMs, lateral positioning errors (typically ~3% of the scanning range) could be identified using a calibration grating and post processing of data. However, the data processing required to do this was somewhat arduous, computationally intensive and does not lend itself to real-time signal processing. To address this, the authors have, within the scope of a recently completed European Metrology Research Programme project [18] and European Metrology Research and Innovation Programme project [19], used optical interferometers to directly measure lateral stage displacements in real time. This can provide both a traceable measurement of the stages position and a map of the scanning errors associated with the scanning and positioning stages. Using position data from interferometers removes any errors that might arise due to unexpected stage motion. Although the introduction of metrology required a larger scanning stage than is typically used for this mode of HS-AFM, the ability to make use of existing, proven optical interferometer configurations (discussed later) made up for the resulting shortcomings of the performance of this larger stage (see later). Nevertheless, use of the interferometers in a high-speed context required the development of high-speed, accurate optical interferometry fringe counting electronics and signal processing techniques.

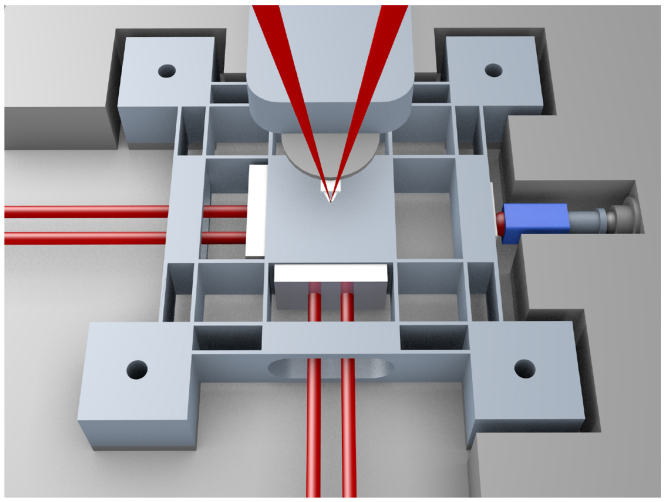

Figure 1. Shows a schematic, not to scale, of the high-speed scanning flexure stage showing mirrors and interferometer beams (in red). A simplified AFM probe is also shown with the converging beams coming from the head. Overall stage size (70 mm × 70 mm).

2. HS-AFM instrument description

The instrument comprises a short-range high-speed scanning stage and a long-range dual-axis slip-stick positioner used with optical interferometers to measure the relative lateral displacement between the tip and sample.

The components that make up the HS-AFM system are mounted on an optical table with pneumatic vibration isolation. They are then enclosed within a Celotex enclosure that kept the temperature stable to within 20 °C ± 0.1 °C in order to comply with ISO 1:2016 [20].

Each component is described here, starting with the high-speed stage which is central to the whole instrument.

2.1. Stage design

In order to provide metrology for measurement of the stage position, the original stage design was modified so that mirrors could be attached to the external faces of the moving component perpendicular to scan directions. A close-up image of the high-speed stage is shown in figure 1. The mirrors are affixed to the sides of the central square platform of the stage and holes were machined into the sides of the frame opposite to facilitate access by interferometer beams from a double pass interferometer. The minimum size of the mirrors was dictated by the beam spacing of the chosen interferometer design and the desired translation of the whole high speed stage to

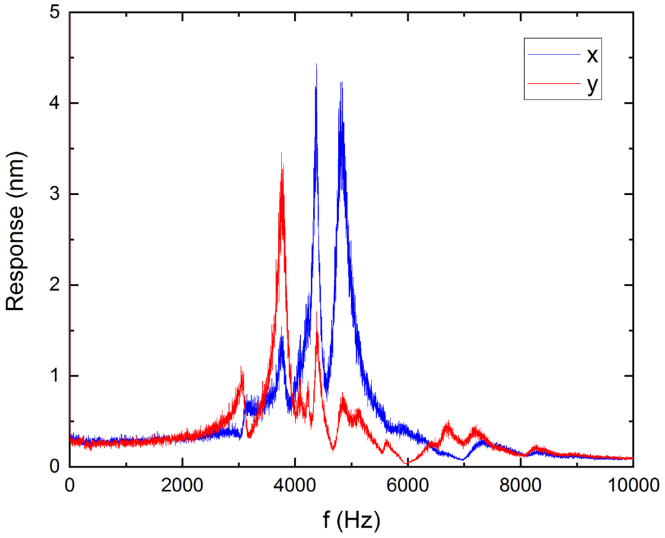

Figure 2. Shows a graph of the resonance curves for the high-speed stage. The first major peaks for the *x* and *y* axes occur at 4.37 kHz and 3.75 kHz, respectively.

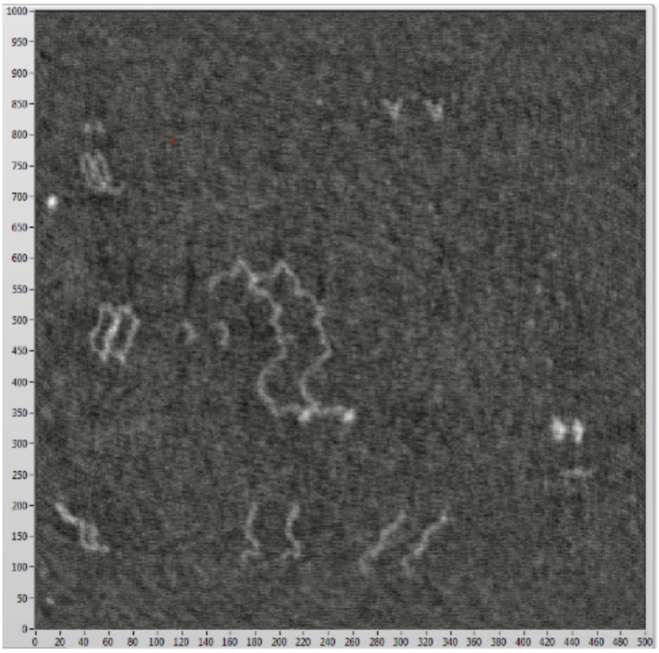

Figure 3. Shows HS-AFM trace and retrace frames superimposed of DNA molecules obtained without the metrological sensors. Image size 4 μm × 4 μm with a Z range of 2 nm.

accommodate large-area scans. The size of mirror required necessitated a larger stage design, (17 mm × 9 mm) central region, than used in previous work [10].

In order to obtain line rates of 1 kHz or higher using this larger stage it was designed to have a high fundamental resonance frequency [4]. This was achieved by increasing the thickness of the flexure elements in the stage to 0.6 mm. Some initial stage modelling was done to determine the feasibility of a larger stage.

A graph showing the measured resonant frequency of the manufactured stage is shown in figure 2. The first major peaks for the *x* and *y* axes occur at 4.37 kHz and 3.75 kHz respectively. The resonances were found by driving the stage with a uniform noise signal and taking an FFT of the stage response [21]. The observed resonances are higher than expected from the simulation. This is likely to be because of additional constraints due to the stage driving mechanism that are unaccounted for by the simulation.

The large size of the mirrors on the high speed stage (16 mm × 9 mm) means that the sample mounting area of the stage is larger than in the case of the previous non-metrological instrument developed by UoB. The consequence of the increased size and hence stiffness of the stage used is that the scan amplitude is limited to typically 4.5 μm × 4.5 μm and the second lateral resonance and the drum mode of the stage are at frequencies that can be observed in the line scans, which can be removed with post processing.

The stage is driven using a stack piezo and voltage amplifier operating in open loop. The stage was therefore susceptible to the piezo actuators hysteresis and non-linearity. Uncorrected, this causes a small offset between trace and retrace images as well as internal spatial distortions within the image. Figure 3 shows an example of the differences between trace and re-trace images when they are superimposed. Note the apparent duplication of the same DNA molecules within the image. In order to be able to correct the image distortion, it is necessary to know the actual position of the stage in *x* and *y* rather than relying on the signals provided to the piezo actuators and assuming a perfect stage response. Although, to some extent, this is achievable by post processing the data, there is a fundamental lack of traceability and internal spatial consistency between the different images due to asymmetric imaging error.

Although the design of the parallel flexures should limit crosstalk between *x* and *y* axes as well as out of plane motion [22] there will, nevertheless, be errors associated with the stage motion. The stage design used represents a compromise between scanning speed, physical dimensions, and stage errors.

To integrate the high-speed scanning stage into a usable HS-AFM system further scanning and positioning elements are needed. Figure 4 shows the five required positioning stages, designated (from bottom to top) as A to E. The cantilever motion detection head (described in section 2.3) is fixed in position above the stage array.

The whole system, excluding the detection head, can be translated in *x* and *y* using stage A in order to align the AFM cantilever laterally with the head. Moving the entire system instead of just the cantilever reduces the number of translation stages included in the measurement loop for the *x* and *y* axis interferometers. Stage B is a wedge type slip-stick stage that moves the high-speed stage and the sample in the vertical axis. This is used to bring the sample into contact with the AFM probe. Stage C, a servo controlled slip stick *x*-*y* stage, provides coarse scanning in the *x* and *y* axes by moving the high-speed scan window across the sample, thus allowing imaging over a larger range than is available with the high-speed stage alone. Stage D is the high-speed stage, already described. Stage E allows the AFM probe to be moved in the vertical direction in

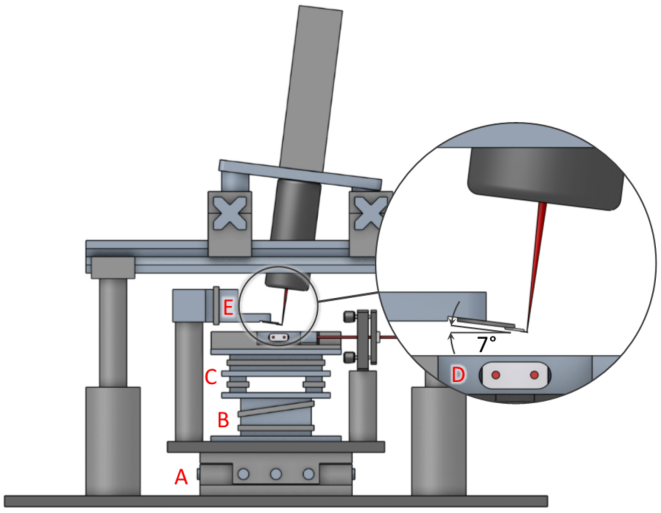

Figure 4. Shows a schematic of the side of the metrological HS-AFM instrument showing the various stages and head. Stage A is used to align the entire system of linear actuators and positioners with respect to the head in order to align the cantilever in the x–y plane. B moves the system in the vertical direction to bring the cantilever in and out of contact. Stage C, is for coarse x–y scanning. Stage D is the high speed stage. Stage E moves the cantilever in the vertical direction in order to align it in z with respect to the head. Note 7° angle of the head away from vertical.

order to properly focus the detection head optics on the back of the cantilever.

2.2. Interferometry for measurement of scanning motion

Optical interferometry is the established route to traceability for dimensional metrology and the last decade has seen many metrological AFMs developed by NMIs [2] in which interferometers are used to traceably measure the displacement of the AFM tip with respect to the sample. To achieve this with the HS-AFM, NPL homodyne plane mirror differential optical interferometers [23] were used in keeping with the NPL MAFM [24]. They have several advantages: their differential configuration reduced the measurement loop and dead path as well as sensitivity to environmental fluctuations. The double pass configuration reduced sensitivity to any yaw rotation about the z axis in the stage as the beams from the interferometer are symmetric about the centre of the stage; any rotation causes a lengthening in one beam path and a reduction in the other. It was expected that this rotation would be significantly greater in the HS-AFM than the errors encountered in a typical high precision stage as used in a metrological AFM. The disadvantage of the differential configuration is the need (as discussed previously) to design a larger stage to accommodate the wider mirrors needed for the two beams as this reduces the potential scanning speed of the stage. The mirrors used had a flatness of $\lambda/10$ ($\lambda = 633$ nm) over 90% of their surface area. The stage mirrors were cut from a larger mirror and care was taken to ensure that the mirrors did not deform during cutting. Since the interferometer has a double pass configuration, not only is the local flatness over the region of incidence of the light spots important, but also the flatness between the points of incidence of the two spots on the mirror surface.

Usually metrological AFMs measure more slowly than normal AFMs. MAFMs tend to make discrete movements followed by a pause to allow the stage to settle before making a series of interferometer readings. These are averaged to reduce the effects of statistical noise, and hence the type A (statistical) uncertainty. The measurement of a high-speed stage with scan speeds of the order of 8 mm s^{-1} therefore presents a challenge in comparison.

Bespoke high-speed electronics were designed that comprised transimpedance amplifiers for the conversion of photodiode currents and conditioning electronics to produce normalised quadrature signals that could be processed using a 16-bit high-speed analogue-to-digital conversion card. The bandwidth of the electronics, 2 MHz, matched the rate of the data acquisition card for position and topography signals. As the HS-AFM is operating in a contact constant-height displacement mode, in the absence of a control loop, the data rate is equal to the lowest bandwidth component of the detector system (i.e. 2 MHz) [4].

Figure 5(a) shows the noise associated with the interferometer and the electronics. This spectrum was taken from data collected with all four beams of one of the plane mirror differential optical interferometers reflected from the same plane mirror. Figures 5(b) and (c) show the total noise in the x–y and z axes respectively. These spectra correspond to RMS noise values of 0.7 nm in the x and y axes and 1.4 nm in the z axis. These spectra (b) and (c) were taken from data collected whilst the system was not in scanning mode and the sample was out of contact. It can be seen that similar features appear at around 100 Hz in figures 5(b) and (c). These are likely to originate from mechanical resonances associated with the system as a whole. Additional features can be seen on the z axis spectrum. These are likely associated with the cantilever and its mounting arrangement; in particular the well-defined peak at 7 kHz is the resonant frequency of the cantilever (Bruker MSNL C). It should be noted that the noise level on a final image will be reduced as the rasterisation process averages over multiple data points per pixel (the exact number depending on the chosen scan parameters and resolution of the rasterised image).

2.3. Detection of cantilever motion

The detection of the cantilever displacement was switched from the commercial laser Doppler vibrometer used in previous work [13] to a custom-made head based on a modified version of an NPL-designed Michelson interferometer [25] that uses corner cubes. The head is shown in figure 6. In this modified interferometer the corner cube in the measurement axis was removed and the beam is instead focused onto the cantilever using a 50× long working distance microscope objective and reflected back into the interferometer being displaced from the original beam path as would have been the case if the corner cube reflector had been used. The outgoing and ingoing beams are not parallel to the axis of the objective; they

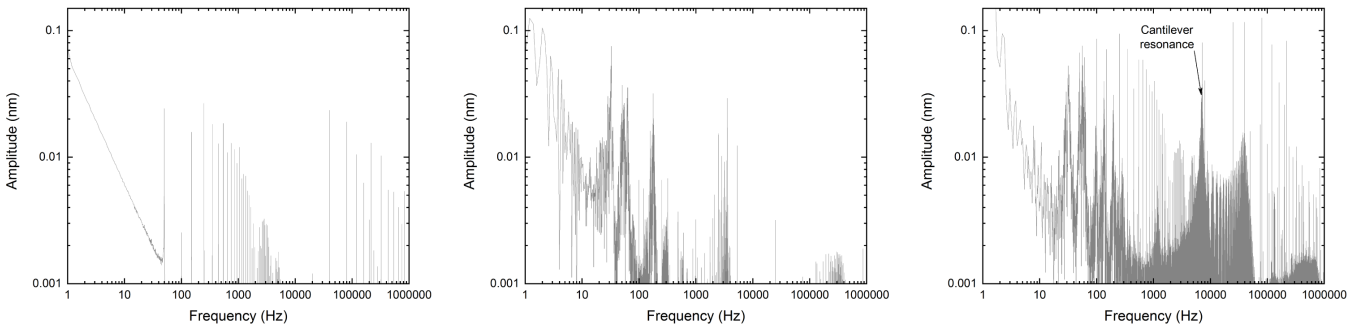

Figure 5. Shows graphs describing the noise associated with the interferometer and the electronics. (a) Noise associated with the electronics, taken from data collected with all four arms of a plane mirror differential optical interferometer reflected from the same plane mirror. (b) Noise associated with horizontal axes. (c) Noise associated with vertical axis. These last two spectra were taken from data collected whilst the system was not scanning.

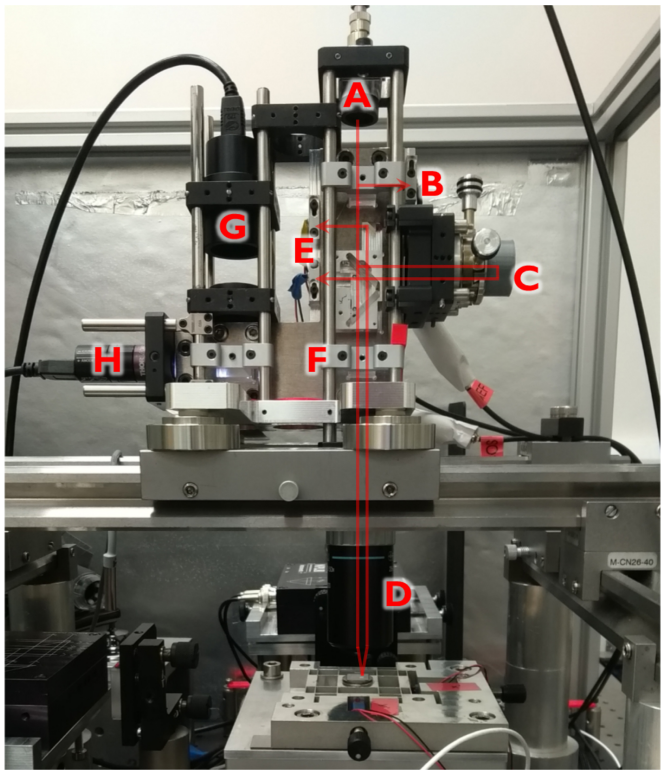

Figure 6. Shows a photograph of the interferometer head mounted above stage assembly with laser beam paths drawn on. A: Fibre-fed collimator; B: Intensity reference photodiode fed by 90:10 beam splitter; C: reference corner cube; D: 50× long working distance microscope objective. E: Interferometer photodiodes; F: Beam splitter for viewing system; G: Camera; H: Illumination source for viewing system. Note that cantilever holder has been removed, the cantilever would be positioned just above the sample where the beams are shown converging.

are focused onto the cantilever at an angle determined by the objective's focal length, a correction is applied when calculating the displacement from the interference signal. A further correction is required to compensate for the fact that the head is tilted with respect to the sample to match the tilt of the cantilever.

In both systems (vibrometer and interferometer) the z motion of the cantilever is recorded relative to a fixed point in the measurement head. This means that z measurements will, in addition to genuine sample topography, contain contributions from sample tilt with respect to the x–y plane, parasitic z motion occurring due to stage errors during x–y scanning and thermal drift. These additional contributions can be removed in post processing. A fully metrological system [24] would measure the cantilever z position relative to the stage (as occurs for x and y). It should be noted that the the switch from vibrometer to interferometer makes little difference to the measurement uncertainty associated with the z data, especially when the post processing steps (described later) are taken into account. The main advantages of the change was that it allowed the use of existing NPL components and the use of the same conditioning electronics as the lateral axes.

2.4. Data collection and scanning

Interferometer signals for all three axes are collected simultaneously at 2 MHz with 16 bit resolution. Fringe counting to convert the raw data into positions was carried out in real time on a PC. Scanning rates were up to 1 kHz for the fast axis and typically 1 Hz for the slow axis, giving a maximum spatial resolution for the x and y interferometers of 4 nm for scan speeds of up to 8 mm s^{-1}. In practice the fast scan frequency was chosen such that the parasitic z motion was reduced, typically frequencies around 760 Hz were found to be suitable. In normal operation the high-speed stage (D) is continuously scanned and then translated using the coarse stage (C) so that larger areas can be imaged.

Each frame can be displayed live with pixels based on measured coordinates rather the drive signal to the piezoelectric actuators. Successive frames can be captured while translating the sample under the cantilever using the long-range slip-stick stage system, and based on the interferometer data combined to produce a larger image. Various scanning paths for the slip stick stage were used. These were generated using the Gwyscan library [26]. It was found that a spiral shaped

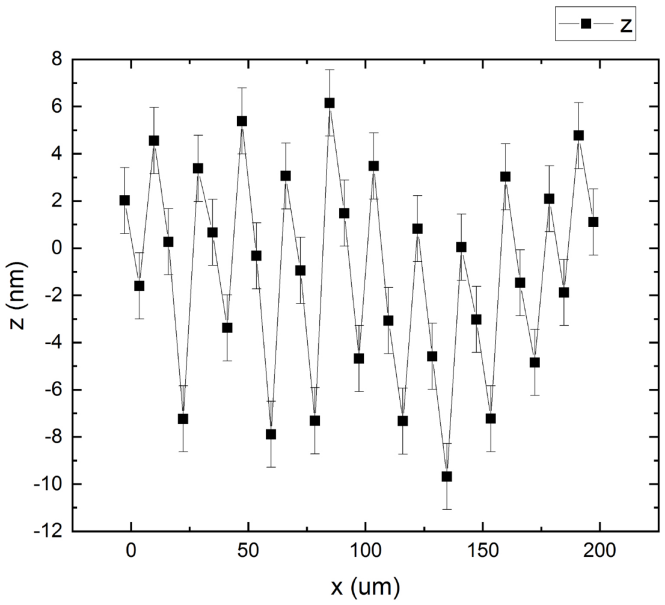

Figure 7. Shows a plot of measured z position of a mirror on the slip stick stage using the interferometer at different (stationary) positions in the x direction. It can be seen that there is deviation from the ideal flat motion by several nanometres.

slip-stick stage scanning pattern was a good choice to quickly build up a large-scale image from the centre outwards.

When scanning across larger areas, explored using the coarse positioners, data is only recorded whilst the slip stick stages are stationary in order to reduce the effects of Z motion from the slip stick stages used for large-area positioning. When the linear stages are moved over ranges of the order of hundreds of micrometres unwanted motion in the vertical (z) direction of the order of several nanometres is observed. This was measured by translating a mirror under the interferometer head. The motion observed was repeatable across multiple areas of the mirror showing that the observed height changes are coming from the stage and not variations in the mirror surface. An example trace over a 200 μm scan range is shown in figure 7. This motion is not identical for each step. To compensate for this motion a post-processing step is used during the formation of large-area images. Frames were collected while the translation stages were static and with a region of overlap between frames. The overlap regions were used to minimise any height offset between adjacent frames [18].

Usually data are recorded in each location for a few seconds giving two to five frames, which can be averaged to reduce statistical noise.

A basic stitching process is used to show the long-range image building up in real time whilst a more complex post processing programme is used to produce the final images. During this post processing interferometer non-linearity can be removed using a Heydemann correction [27] and environmental effects on the refractive index of air and hence the laser wavelength can be accounted for using an Edlen correction [28].

2.5. Image processing

Each acquisition of data collects the instantaneous traceable x, y, z coordinates, together with the sine and cosine interferometer data and a timestamp to allow for any additional corrections. If needed, the time stamp can be used to correct for drift in the system [26], should it be significant. The collection of x, y, z data has the benefit that three dimensional image data from sequential high-speed images can, in the ideal case, be processed together and immediately rasterised in order to produce a large-area data set of the surface topography. The rasterisation interpolates unequally spaced data onto a grid of equally spaced data points.

The x and y coordinates obtained with the interferometers are normalised and coerced onto a grid of arbitrary size. Typically this grid has fewer pixels than there are data points in the raw data. As such each pixel on the coerced grid is filled by more than one point from the raw data. Using this grid two image arrays are created. The first image array records the sum of all z values at that pixel (the cumulative array) and in the second the number of data points at the pixel (the pixel stack array). Dividing the first value by the second produces the average z value for that pixel. This improves the statistical validity for the value of a given pixel and leads to a noise reduction (see later). Typically a single frame rasterised onto a 512×512 pixel image has a mean of 24 data points per pixel.

This procedure on its own is used to generate images from single frames of data and to produce the real-time preview images during scanning. The metrological nature of the x and y stage measurements means no further manipulation of the x and y data is required when combining frames to produce a larger image. The z data however requires further processing stages in order to generate a good quality composite image. This processing is to compensate for the parasitic z motion of the HS stage, errors in the slip stick coarse scanning stage and any effect that might be caused by sample tilt in addition to any thermal drift. These additional corrections are applied during post-processing.

First an image grid is defined using the full x–y range of all the frames to be stitched. Next each frame is individually rasterised into its final location within the large image grid using the same procedure as for single frame images described above. Then a subset of the large grid that corresponds to the added frame is taken. This subset is then stored along with the position data for its location in the large image grid.

Once image subsets for all of the frames have been obtained they are then overlaid and averaged to find the common background shape of the frames. Averaging over large numbers of frames, each from a point on the sample, should remove any contribution from genuine topography and leave behind the common background caused by the parasitic z motion in the high-speed stage. This common background can then be subtracted from each subset, leaving behind the genuine topology but removing contributions from parasitic (Z axis) stage motion. This subtracted background is displayed in software. A visual examination of the background image can immediately show if the averaging has worked or the background contains topology data thus making it unsuitable for subtraction.

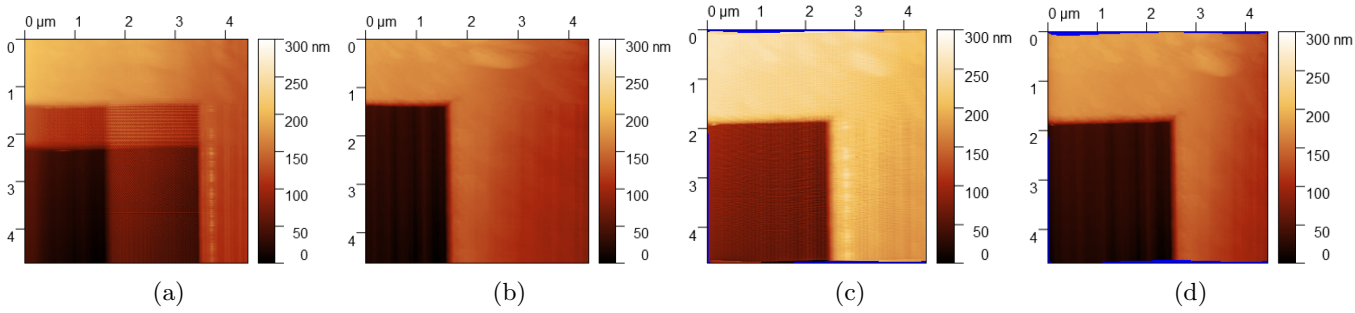

Figure 8. Region of an orthogonal grating. Images generated with *x*–*y* data taken from (a) piezo driving voltage signals, trace and retrace in both axes (b) voltage signals, trace only in both axes (c) interferometer signals, trace and retrace in both axes (d) interferometer signals, trace only in both axes. *z* data is the same for all images. Blue regions (at the top of images c and d) represent blank space due to non-straight image edges. Note that the hysteresis associated with the piezos leads to both ghosting of trace and retrace and spurious curvature, problems both of which have been eliminated by the real-time interferometer measurements.

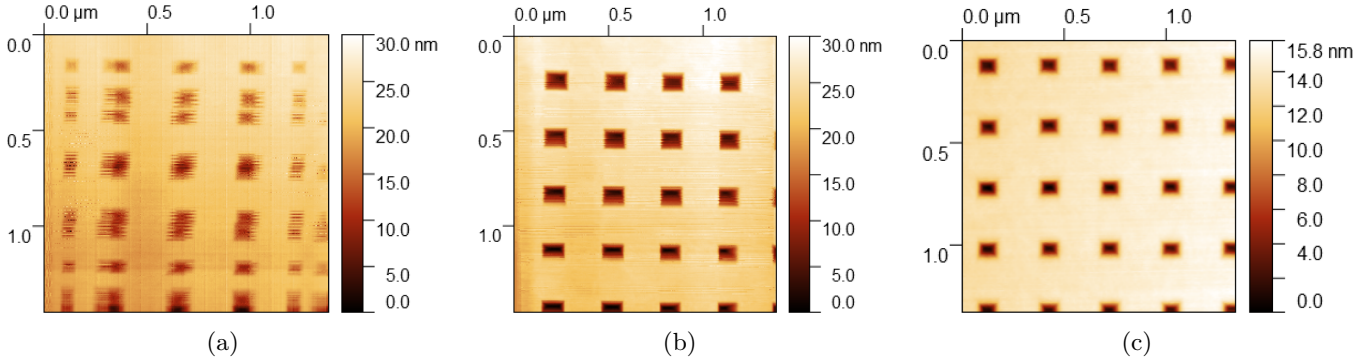

Figure 9. Images of a section of 300 nm 2D pitch standard. (a) Data taken from piezo driving signals. (b) Data taken from interferometer signals. (c) Image of a similar region taken using NPL's metrological AFM. Note that the MAFM uses a blunter probe meaning the image is less well defined and that the inverted pyramid structures appear shallower.

To compensate for errors in the slip stick stage, misalignment of the scanning planes of the coarse and high-speed stages and other *z* axis drifts *z* stitching is required. To do this the mean offset between overlapping frames is calculated. This offset is then minimised in order to vertically align the data of adjacent frames. The stitching process can be carried out either sequentially (one frame added at a time) or globally (all frames considered simultaneously via an optimisation algorithm) [18].

Before the stitching process the data is filtered to remove frames including motion of the slip stick stage by rejecting frames that have overall size greater than a specified value (chosen based on expected sample/scan characteristics) in all three axes.

3. Results and discussion

Images of selected samples were obtained in order to demonstrate the features and performance of the HS-AFM system. The images in figure 8 demonstrate the errors present in the high-speed stage. A region of a grating containing straight, orthogonal features was imaged and data simultaneously recorded for the high-speed stage driving voltage and interferometer signals. It can be seen in the two images generated by placing data in pixels using the phase corrected drive voltage signals that significant distortion is present. This is as expected, given the design of the stage, manifesting both as misalignments between the trace and retrace (due to piezo hysteresis) in both axes and as distortion that results in straight lines becoming curved (due to crosstalk between stage axes). It can be seen in the images generated from the interferometer data, that the trace and retrace images are now aligned.

In order to demonstrate the metrological nature of the *x*-*y* position measurements, a two dimensional calibration grating with a nominal pitch of 300 nm (Nanosensors 2D300) was measured. Figure 9 shows a comparison between images taken using the HS-AFM stage drive signals, the HS-AFM interferometers and NPL's metrological AFM (MAFM). The only post processing applied to the HS-AFM interferometer image was the image rasterisation. To compare the performance in the *x* and *y* axes, average line profiles were taken from both the interferometric HS-AFM image and the MAFM image. These average profiles were fitted to a sine function to determine the pitch value. The pitch results are shown in table 1. It can be seen that the measurements agree within the error on the fit. Additionally, it was found that assessment of the orthogonal nature of the grid lattice using Gwyddion's measurement tools showed that both the HS-AFM and MAFM frames gave the correct angle of 90° to within the resolution of the lateral pixel size.

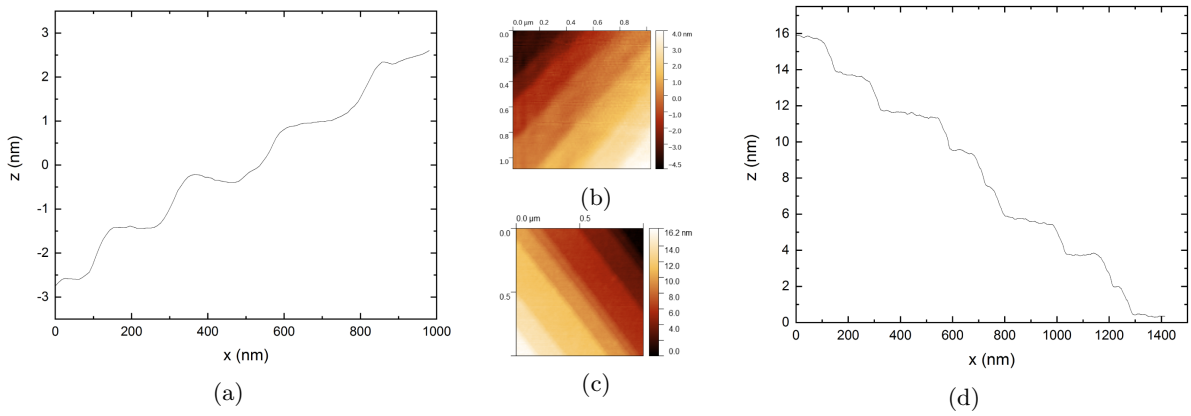

Figure 10. Images of 1.5 nm step height taken on (a, b) the HS-AFM and (c, d) NPL's metrological AFM alongside typical profiles through the images.

Table 1. Pitch measurement results for 2D300 grating from High-speed and NPL's metrological AFMs. The measurements from each AFM agree within the errors on the fit and are close to the nominal 300 nm spacing of the sample.

	MAFM	HS-AFM
X axis	(301.6 ± 1.6) nm	(298.8 ± 1.5) nm
Y axis	(300.6 ± 1.3) nm	(303.0 ± 1.6) nm

To demonstrate the vertical resolution of the HS-AFM, a 1.5 nm silicon carbide atomic step height standard was imaged. Figure 10 shows the recorded image, again compared with a similar image recorded on NPL's metrological AFM. Both images show single atomic steps. Processing of the HS-AFM data included separation of the forward and reverse scans, subtraction of the background due to non-ideal stage motion and rasterising the data with pixel averaging. A small section was cropped from the frame to highlight the relevant features.

The ability to stitch frames together and consequently image larger areas is demonstrated in figure 11. This composite image covers an area of 500 µm × 80 µm and is made up of 3825 individual HS-AFM frames with an approximate overlap of 2 µm between adjacent frames. It should be noted that each individual HS-AFM frame can have as many as 2 million data points. To obtain a similar sized image having an equivalent data density using a state of the art conventional AFM would have taken over three days compared with a little over two hours with the HS-AFM system. Figure 12 shows a smaller stitched area, this time of an 8 nm step height sample. This image is 24 µm × 16 µm made up of 229 smaller images. The line profile shows that despite the post processing to remove parasitic z motion from the data there are still some imperfections (manifesting as high frequency roughness in the low regions) of ~± 0.5 nm that arise during stitching of the individual frames.

The stitched images are positioned in x and y only by use of the interferometer data. It can be seen that this produces well-aligned images demonstrating the ability to measure over long ranges. The coarse scan path used to collect this data followed a lissajous pattern. This results in multiple time separated passes over each area of the image. The good alignment of the data means this results in no additional ghosting or blurring within the image.

This ability to combine images in x and y based solely on the interferometer measurements without additional computation to calculate stitching offsets is one of the key advantages of a fully metrological system in those axes.

The stability of the image is further demonstrated by the images in figure 13. Here two frames of the same region collected 1.5 hours apart are shown. This time scale is about that over which a large-area scan might be taken. The regions are identified from the absolute X and Y position values returned from the optical interferometers and it can be observed that, although the region being imaged changed slightly due to mechanical drift in the stage system, the features in the image line up in the two images (demonstrated by the subtracted image). This shows that the optical interferometric measurement system itself is stable and free from significant drift over the relevant timescales. What is also noticeable is the lack of any effects due to tip wear. At 1 frame per second the tip scans a distance of 9 mm in each frame. During the 1.5 hours time period between the two frames displayed, the tip would have travelled 48.6 m at an average speed of 9 m s^{-1}. This is in contrast to tip wear observed using conventional AFMs [29], where tip wear is evident after a few images. It is worth noting that, tip sample interaction as the cantilever moves across the sample at high-speeds has been found to make use of a fluid dynamical lubrication effect. This protects both the sample and the resolution achievable using the AFM tip [14] even as the cantilever passes over large features in the absence of a per pixel electromechanical control loop. [13]

3.1. Uncertainties

It is worth re-iterating that the aim of this instrument is to bring metrology to an HS-AFM and not to develop a top-level NMI instrument. As such, although the uncertainties associated with both the instrument and data processing are considered here, they are in some cases derived empirically from results presented in this paper rather than from a fundamental

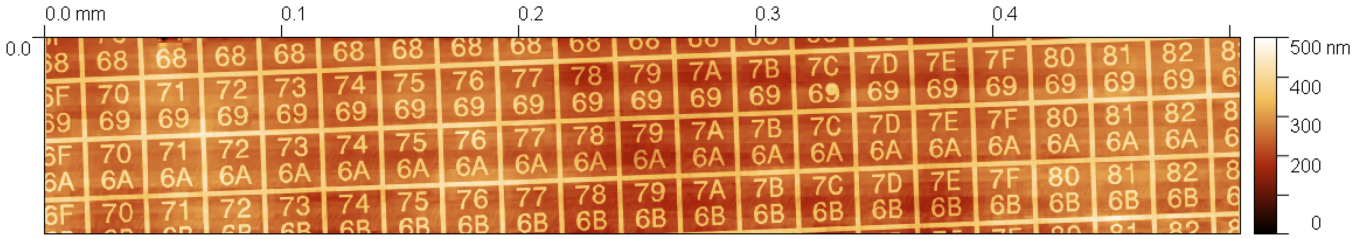

Figure 11. : Stitched image of numbered grating. 3825 frames, 2 µm overlap between frames, 500 µm × 80 µm. 2.4 billion data points, rasterised to 1024 pixels along long edge. The full image took a little over 2 hours to capture.

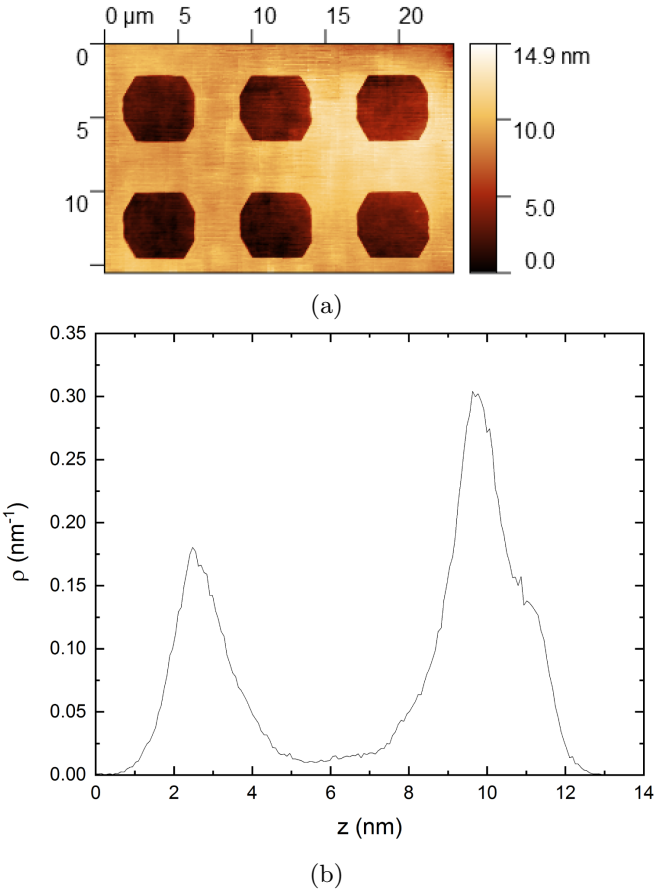

Figure 12. (a) Composite image of a nominal 8 nm step height grating. Lissajous scan path, 229 frames, 72.1 million data points, 24 µm × 16 µm, rasterised to 512 pixels along long edge. The coarse scan path used to collect this data followed a lissajous pattern resulting in data overlaps of up to 100% in the central region. The full image took around 3.5 minutes to capture. (b) Histogram of data points showing two defined levels. The first peak has a fitted centre at 2.66 nm and a standard deviation of 0.62 nm. The second peak has a fitted centre at 9.87 nm and a standard deviation of 0.89 nm. This gives the height of the structure as 7.2 nm. A measurement with the NPL MAFM gave a distribution with similar peak widths and shapes and a height that agreed within the associated uncertainties. Thus any broadening of the peaks is likely due to genuine sample topology rather than uncertainty in the HS-AFM.

model. It also worth noting that the main focus on metrology improvements was on the lateral (*x*-*y*) axes.

The uncertainties associated with metrological AFMs (AFMs with interferometers) have been considered [24] and apply to the instrument described in this paper as well. The traceability of the measurements is derived from the combination of the stabilised helium neon lasers and the interferometers used. The stability of the laser frequency is of the order of a few parts in 10^9. This contribution to the measurement uncertainty is usually dwarfed by the noise measured in the three interferometer axes and interferometer non-linearity (< 0.1 nm); in this case noise was 0.7 nm in x and y and 1.4 nm in z. However, the high data density and averaging process to rasterise the images leads to an effective reduction in noise.

With the high-speed AFM there are additional sources of uncertainty that need to be considered; in the x and y axes this includes rotation of the scanning stage. In the z axis these include unwanted vertical motion of the high speed stage, the long range slip stick stage when moving between fixed positions and any contribution due to stitching.

The total contribution to uncertainty of the instrument must be considered on a case by case basis as they are dependent on range and speed settings. As an example, the data shown in figures 9 and 12 i.e. the pitch and step height can be used to confirm that the compensation for the unwanted z motion when stitching the images is adequate as the images compare favourably with those from the metrological AFM. The image of the 8 nm step height shows an effective noise level of 0.5 nm albeit it is combined with any surface roughness on the samples.

The stage mirrors are attached to the central square of the HS-AFM stage. Errors during the wire eroding of the stage could lead to a non orthogonality between the mirrors of 3×10^{-4} rad. Over the 4 µm scan range this corresponds to an error of 1.6 nm. This does not take into account any twisting of the stage during the measurement. To measure this a high bandwidth autocollimator would be needed. Since one was not available we made an estimate by looking at the orthogonality of the images of the two dimensional 300 nm grating shown in figure 9 where no appreciable difference was observed between the HS-AFM image and the MAFM image to within the uncertainty associated with data processing in Gwyddion [30].

Regarding the vertical axis where the cantilever position is measured using the interferometer, the stability of the laser is similar to that of the lasers for the x and y axes. Figure 5(c) shows the noise associated with the z axis. Corrections have to be made for the difference in path between light reflected from the corner cube and light focused by the objective lens and reflected from the plane mirror surface of the cantilever. The measurements of the 8 nm step height shown in figure 12

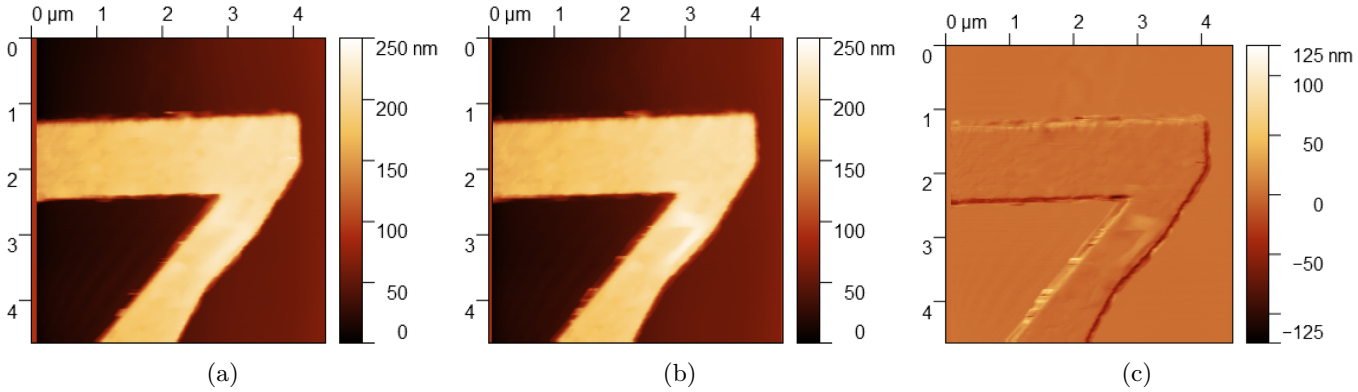

Figure 13. (a and b) Images of the same region of a sample taken 1.5 hours apart, this time is comparable to that required to capture stitched images with sizes of 100 s of µm. (c) The result when (b) is subtracted from (a). All images are on the same *x*-*y* grid. It can be seen that the measured features line up in the two images. Taking a line profile across the edges visible in subtracted image (c) showed the overall lateral drift to be of the order 0.1 µm, insignificant compared to image sizes of 100 s of micrometres.

shows that results are obtained that are in agreement with those from the metrological AFM within the respective uncertainties. It should be noted that further uncertainty is introduced by the stitching process for large images, however this uncertainty can be removed when observing small scale features by taking measurements from the individual frames instead of the composite image.

4. Conclusions

The addition of metrology removes the effects of distortions due to piezo actuator effects and leads to real-time traceable lateral scan data. This in turn permits large composite images to be constructed with no additional data processing steps required, in comparison to non-metrological systems. The use of the NPL interferometer for the *z*-axis detection gives direct traceablity. The stitching required to build large images is relatively straightforward; taking a large set of non-equally spaced data points and rasterising it into a single image. The high speed of the AFM together with the higher lateral resolution of the AFM in comparison with optical techniques is a clear advantage opening up the possibility of looking at millimetre sized areas with nanometre resolution. This is particularly useful for samples that cannot be accommodated in a scanning electron microscope. While there are still improvements that can be made to the system, the advantages are clearly demonstrated.

Acknowledgments

AY and EH would like to thank Rob Hornby and Sarah Sun of NPL for their help with providing code used for image stitching and scan path generation.

The research was supported by EURAMET joint research project ‘Six degrees of freedom receiving funding from the European Community’s Seventh Framework Programme, ERA-NET Plus, under Grant Agreement No. 217257 and from the EMPIR programme co-financed by the Participating States and from the European Unions Horizon 2020 research and innovation programme. Dr Payton and Dr Picco gratefully acknowledge the financial support of the Royal Academy of Engineering and Freddie Russell-Pavier thanks the EPSRC and NPL for financial support.

Disclaimer

The naming of any manufacturer or supplier by NPL, The University of Bristol or CMI in this scientific journal shall not be taken to be either NPL’s, The University of Bristol’s or CMI’s endorsement of specific samples of products of the said manufacturer, or recommendation of the said supplier. Furthermore, NPL, The University of Bristol and CMI cannot be held responsible for the use of, or inability to use, any products mentioned herein that have been used by them.

ORCID iDs

Edward Heaps https://orcid.org/0000-0002-1794-1603
Andrew Yacoot https://orcid.org/0000-0001-6740-821X
Freddie Russell-Pavier https://orcid.org/0000-0002-2150-6989
Petr Klapetek https://orcid.org/0000-0001-5241-9178

References

[1] Danzebrink H U, Koenders L, Wilkening G, Yacoot A and Kunzmann H 2006 Scanning force microscopy for dimensional metrology *CIRP Ann. Manuf. Technol.* **55** 841–78
[2] Yacoot A and Koenders L 2011 Recent developments in dimensional nanometrology using AFMs *Meas. Sci. Technol.* **22** 122001
[3] Dai G, Koenders L, Fluegge J and Hemmleb M 2018 Fast and accurate: high-speed metrological large-range AFM for surface and nanometrology *Meas. Sci. Technol.* **29** 054012
[4] Payton O D, Picco L and Scott T B 2016 High-speed atomic force microscopy for materials science *Int. Mater. Rev.* **61** 473–94

[5] Liu L, Wu S, Pang H, Hu X and Hu X 2019 High-speed atomic force microscope with a combined tip-sample scanning architecture *Rev. Sci. Instrum.* **90** 063707
[6] Keyvani A, Sadeghian H, Goosen H and van Keulen F 2015 Transient tip-sample interactions in high-speed AFM imaging of 3D nano structures *Metrol., Insp., Process Cont. Microlithogr. XXIX* **9424** 94242Q
[7] Ando T 2012 High-speed atomic force microscopy coming of age *Nanotechnology* **23** 062001
[8] Ando T 2019 High-speed atomic force microscopy *Current Opinion in Chemical Biology* **51** 105–12
[9] Russell-Pavier F, Picco L, Day J C C, Shatil N R, Yacoot A and Payton O 2018 'Hi-Fi AFM': high-speed contact mode atomic force microscopy with optical pickups *Meas. Sci. Technol.* **29** 105902
[10] Mikheikin A *et al* 2017 DNA nanomapping using CRISPR-Cas9 as a programmable nanoparticle *Nat. Commun.* **8** 1665
[11] Schitter G and Rost M J 2008 Scanning probe microscopy at video-rate *Mater. Today* **11** 40–8
[12] Ando T, Uchihashi T and Kodera N 2013 High-speed AFM and applications to biomolecular systems *Ann. Rev. Biophys.* **42** 393–414
[13] Payton O, Picco L, Miles M, Homer M E and Champneys A R 2012 Improving the signal-to-noise ratio of high-speed contact mode atomic force microscopy *Rev. Sci. Instrum.* **83** 083710
[14] Picco L M, Dunton P G, Ulcinas A, Engledew D J, Hoshi O, Ushiki T and Miles M J 2008 High-speed AFM of human chromosomes in liquid *Nanotechnology* **19** 384018
[15] Payton O, Picco L, Champneys A R, Homer M E, Miles M and Raman A 2011 Experimental observation of contact mode cantilever dynamics with nanosecond resolution *Rev. Sci. Instrum.* **82** 043704
[16] Klapetek P, Picco L, Payton O, Yacoot A and Miles M 2013 Error mapping of high-speed AFM systems *Meas. Sci. Technol.* **24** 025006
[17] Klapetek P, Valtr M, Picco L, Payton O, Martinek J, Yacoot A and Miles M 2015 Large area high-speed metrology SPM system *Nanotechnology* **26** 065501
[18] PTB 2019 Metrology for movement and positioning in six degrees of freedom (https://www.ptb.de/emrp/ind58-consortium.html)
[19] PTB 2019 Traceable three-dimensional nanometrology (https://www.ptb.de/emrp/15sib09-project.html)
[20] ISO 1:2016: *CH Geometrical Product Specifications GPS—Standard Reference Temperature for the Specification of Geometrical and Dimensional Properties* (International Organization for Standardization)
[21] Yuen K Y, Aphale S and Reza Moheimani S 2009 Design, identification, and control of a flexure-based XY stage for fast nanoscale positioning *IEEE Trans. Nanotechnol.* **8** 46–54
[22] Fantner G E *et al* 2006 Components for high speed atomic force microscopy *Ultramicroscopy* **106** 881–7
[23] Yacoot A and Downs M J 2000 Measurement Science and Technology The use of x-ray interferometry to investigate the linearity of the NPL Differential Plane Mirror Optical Interferometer *Meas. Sci. Technol.* **11** 1126–30
[24] Haycocks J and Jackson K 2005 Traceable calibration of transfer standards for scanning probe microscopy *Precis. Eng.* **29** 168–75
[25] Downs M and Rowley W 1993 A proposed design for a polarization-insensitive optical interferometer system with subnanometric capability *Precis. Eng.* **15** 281–6
[26] Klapetek P, Yacoot A, Grolich P, Valtr M and Nečas D 2017 Gwyscan: a library to support non-equidistant scanning probe microscope measurements *Meas. Sci. Technol.* **28** 034015
[27] Heydemann P L M 1981 Determination and correction of quadrature fringe measurement errors in interferometers *Appl. Opt.* **20** 3382–4
[28] Birch K P and Downs M J 1994 Correction to the Updated Edlén Equation for the Refractive Index of Air *Metrologia* **31** 315–16
[29] Bakucz P, Yacoot A, Dziomba T, Koenders L and Krüger-Sehm R 2008 Neural network approximation of tip-abrasion effects in AFM imaging *Meas. Sci. Technol.* **19** 065101
[30] Nečas D and Klapetek P 2012 *Central Eur. J. Phys.* **10** 181–8